

Fast trajectory reconstruction techniques for the large acceptance magnetic spectrometer VAMOS++

A. Lemasson*, M. Rejmund

GANIL, CEA/DRF - CNRS/IN2P3, Bd Henri Becquerel, BP 55027, F-14076 Caen Cedex 5, France

Abstract

The large angular and momentum acceptance magnetic spectrometer VAMOS++, at GANIL, France, is frequently used for nuclear structure and reaction dynamics studies. It provides an event-by-event identification of heavy ions produced in nuclear reactions at beam energies around the Coulomb barrier. The highly non-linear ion optics of VAMOS++ requires the use of the heavy ion trajectory reconstruction methods in the spectrometer to obtain the high-resolution definition of the measured atomic mass number. Three different trajectory reconstruction methods, developed and used for VAMOS++, are presented in this work. The performances obtained, in terms of resolution of reconstructed atomic mass number, are demonstrated and discussed using a single data-set of fission fragments detected in the spectrometer.

1. Introduction

Magnetic spectrometers are very powerful tools to identify and characterize nuclei produced in nuclear collisions. In the recent years, large acceptance magnetic spectrometers like VAMOS++ [1, 2] at GANIL and PRISMA [3] at LNL Legnaro have significantly contributed to the advances in the domain of nuclear structure and reaction mechanism studies. They allow the isotopic identification and therefore the clean selection of reaction products on an event-by-event basis. The above-mentioned spectrometers are particularly suited for reaction at the beam energies near the Coulomb barrier, where a large angular and momentum acceptance is necessary for efficient collection of the nuclear reaction products of interest. However, a large angular and momentum acceptance is related to large sizes of optical elements, composing the spectrometer, which often result in a design that exhibits a highly non-linear optics. Therefore, ray-tracing techniques for a trajectory reconstruction [1, 2], are required, leading to the determination of the magnetic rigidity and related observables for the detected heavy ions.

The isotopic identification, in terms of atomic mass number A and atomic number Z , is the key issue as far as the magnetic spectrometers are concerned. The basic measurement provided by a magnetic spectrometer is the magnetic rigidity $B\rho$ of the ion, it is proportional to the position in the dispersive plane of the dipole magnet. The magnetic rigidity is related to the velocity v and mass-over-charge ratio (A/q), where q is the atomic charge state. The measurement of the velocity v allows to obtain the corresponding mass-over-charge ratio (A/q). The measurement

of the atomic mass number A requires the measurement of the atomic charge state q . Numerous spectrometers are used at high beam energies, from few tens to hundreds of MeV/A, so that the heavy ions of interest can be obtained in a fully stripped charge state, that is $q = Z$. Note that the energy necessary to reach the fully stripped charge state for a given atomic number Z increases with Z . In this case the measurement of the correlation between the energy loss of the ion ΔE and its time-of-flight t or velocity v , is often sufficient to determine the atomic charge state $q = Z$ and thus also the corresponding atomic mass number A [4, 5]. However, at energies near the Coulomb barrier, heavy ions have lower atomic charge state $q < Z$, with wide statistical distributions. In this case, the measurement of the total energy E_{tot} of the incoming ion is necessary. The relation between the total energy E_{tot} and atomic mass number A combined with the measurement of magnetic rigidity $B\rho$ allows to determine the atomic charge state q , for each ion individually. Due to the large angular and momentum acceptance, the measurement of the correlation between the energy loss ΔE and the total energy E_{tot} or velocity v are necessary to obtain the atomic number Z [6]. Additionally, at lower beam energies, it is mandatory to minimize the effective thickness of every detector, through which the heavy ions are passing, the window thickness in particular, to reduce the related unmeasured energy losses.

VAMOS++ has been fruitfully used for a wide range of experiments covering (i) particle and γ -ray spectroscopy using direct transfer [7–16], multi-nucleon transfer: [17–33], fission [6, 34–54], and Coulomb excitation [55] (ii) fission [56–66] and reaction dynamics [67–72].

In this paper, three different trajectory reconstruction methods elaborated for the VAMOS++ magnetic spec-

*Corresponding author

Email address: antoine.lemasson@ganil.fr (A. Lemasson)

trometer throughout the years of operation are described. The achieved performances will be discussed in terms of resolution of the reconstructed atomic mass number.

2. VAMOS++ spectrometer

The layout of the VAMOS++ spectrometer is presented in Fig. 1(a). The optical elements of the VAMOS++ spectrometer [1] consist of two large aperture magnetic quadrupoles (Q1, Q2) for focusing heavy ions vertically and horizontally, respectively and a magnetic dipole (D) for dispersing heavy ions horizontally. The Wien Filter (WF) placed in-between the two magnetic quadrupoles and the magnetic dipole, is not used in the present work.

Due to the large angular and momentum acceptance of VAMOS++ the corresponding ion-optics is highly non-linear, as will be demonstrated in Sec. 3, and a direct measurement of horizontal ion coordinate at the dispersive focal plane is insufficient to determine the magnetic rigidity $B\rho$ of the transmitted heavy ions. Therefore, more complex measurements of final coordinates, using the heavy ion tracking detectors, is necessary to perform ray-tracing and determine the magnetic rigidity $B\rho$, the velocity vector \vec{v} and the trajectory length l . Typically, the focal plane detection system of VAMOS++ included two heavy ion tracking detectors, either secondary electron detectors (SeD) [1, 73] or drift chambers [1, 2], providing the measurement of horizontal and vertical coordinates ($x_f, \theta_f, y_f, \phi_f$), where the index f refers to final focal plane coordinates. Note, that the final focal plane coordinates were obtained on the image focal plane placed 7600 mm away from the target. Additionally, an ionization chamber, either standalone [6] or combined with a plastic detector [7] or silicon wall detectors [1, 2] were used to provide the measurement of the energy loss and total energy correlation $\Delta E - E_{tot}$. The stop for the time-of-flight measurement was provided by the plastic detector [7], secondary electron detectors (SeD) [1, 73] or multi-wire proportional counter (MWPC) [2, 6]. For the start for the time-of-flight (t) measurement, during the early years of operation, the cyclotron radio-frequency was used [1]. Since 2011, the multi-wire proportional counter, at the entrance of VAMOS++, (MWPC) [2] and since 2016 the dual position sensitive MWPC telescope (DPS-MWPC) [74] were used. The DPS-MWPC in addition to the timing signal provided the measurement of initial horizontal and vertical coordinates at the target ($x_i, \theta_i, y_i, \phi_i$), where the index i refers to initial coordinates at the target.

Schematic view of the VAMOS++ detection system, used to obtain the data presented in this paper [6], is shown in Fig. 1(b). The DPS-MWPC telescope was placed at the entrance of VAMOS++. It consists of a pair of MWPCs, placed in a common gas volume. Each of MWPCs provides a precise timing signal as well as horizontal (x) and vertical (y) position. Therefore, a combination of all position measurements results in a determination of the interaction

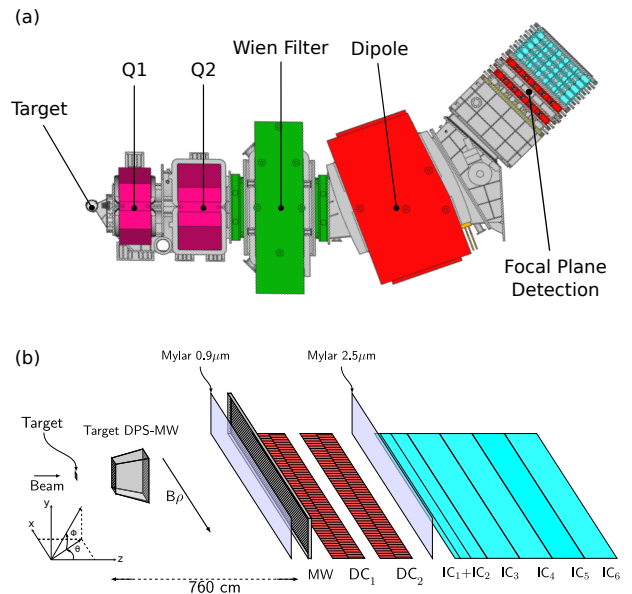


Figure 1: (a) Schematic view of the elements of the VAMOS++ spectrometer. The optical elements: two magnetic quadrupoles Q1 and Q2 for a vertical and horizontal focussing, Wien Filter WF (unused) and magnetic dipole D for horizontal dispersion. (b) Schematic view of the VAMOS++ detection system. θ is the angle between the z -axis and the projection of the velocity vector of the trajectory on the xz plane (symmetry plane), ϕ refers to the angle between the velocity vector and its projection on the xz plane. A dual position sensitive multi-wire proportional counter telescope (DPS-MWPC) is placed at the entrance of the spectrometer. At the focal plane, a multi wire proportional counter focal plane (MWPCFP), two drift chambers and segmented ionization chambers. Two Mylar windows used to isolate the detection gases are also shown.

position at the target (x_i, y_i) and the corresponding scattering angles (θ_i, ϕ_i). The focal plane detection system of VAMOS++ [2], has an active area of $1000 \times 150 \text{ mm}^2$ and consists of multi wire proportional counter focal plane (MWPCFP), two drift chambers and segmented ionization chamber. The MWPCFP, is 20-fold segmented in horizontal direction into sections and provides the timing signal for the measurement the time-of-flight (t). Each drift chamber measures the horizontal and vertical position that are used to obtain position (x_f, y_f) and angles (θ_f, ϕ_f) at the image focal plane.

The ionization chamber, is five-fold segmented in horizontal direction to improve its counting rate capabilities. It is also eight-fold segmented in depth. The atomic number Z of the heavy ion is obtained from the correlation of the measured ΔE and E_{tot} , see also Ref. [6].

The complete identification of the heavy ion using VAMOS++ spectrometer is obtained from the following rela-

tions:

$$v = \frac{l}{t}, \beta = \frac{v}{c}, \gamma = \frac{1}{\sqrt{1 - \beta^2}}$$

$$(A/q) = \frac{B\rho}{3.107 \cdot \beta \cdot \gamma}$$

$$A_{(E_{tot}, \gamma)} = \frac{E_{tot}}{931.494 \cdot (\gamma - 1)}$$

$$q_{int} = \left\lfloor \frac{A_{(E_{tot}, \gamma)}}{(A/q)} + 0.5 \right\rfloor$$

$$A = (A/q) \cdot q_{int}$$

where v corresponds to the velocity in cm/ns, l the trajectory length in cm, t the time-of-flight in ns, c the speed of light, $B\rho$ the magnetic rigidity in Tm, E_{tot} the total energy in MeV, $A_{(E_{tot}, \gamma)}$, is the atomic mass measured from total energy and velocity with resolution arising from the total energy resolution, (A/q) the mass-over-charge ratio, q_{int} is the integer value of the atomic charge state and $\lfloor x + 0.5 \rfloor$ is the nearest integer value of x , A the atomic mass number.

3. Ion-optics and ray tracing

The trajectory of an ion along the spectrometer, can be described using the standard ion optics formalism using a six parameter vector $\vec{l} = (x, \theta, y, \phi, l, \delta)$ defined relative to a reference trajectory vector $\vec{l}_0 = (0, 0, 0, 0, l_0, 1)$ for an ion with the reference magnetic rigidity $B\rho_0$. The parameters x and y correspond to two transverse distances from the reference trajectory, see Fig. 1(b), θ is the angle between the z -axis and the projection of the velocity vector of the trajectory on the xz plane (symmetry plane), ϕ refers to the angle between the velocity vector and its projection on the xz plane, $\delta = B\rho/B\rho_0$ defines the relative magnetic rigidity and l is the path length from the target to the image focal plane.

For ray-tracing purposes, a set of vectors in the initial phase space starting at the origin $x_i, y_i = 0$ (assuming a point-like source) with well defined angles $(\theta_{i_k}, \phi_{i_k})$ and relative magnetic rigidity (δ_{i_k}) , $\vec{l}_{i_k} = (0, \theta_{i_k}, 0, \phi_{i_k}, 0, \delta_{i_k})$, were generated. These vectors exceed a maximum angular and momentum acceptance of the spectrometer and are defined within the range $\Delta\theta, \Delta\phi = \pm 160$ mrad and $\Delta\delta = \pm 0.3$. The generated density of initial vectors depends on the targeted resolution of the trajectory reconstruction $(\theta, \phi, \delta, l)$ and the trajectory reconstruction method applied (see below). The trajectories of the ions in VAMOS++ were calculated using ray-tracing code ZGOUBI [75]. Realistic field descriptions for each magnetic element were considered in the calculation by incorporating median plane field maps issued from the 3D field maps generated using electromagnetic computation code TOSCA [76]. The code ZGOUBI traces an ion through a system of magnetic fields and calculates the final coordinates numerically by integrating the equation of motion in a magnetic

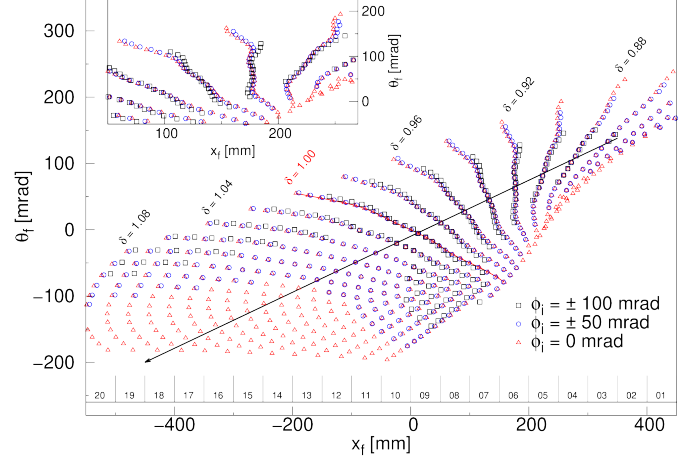


Figure 2: Aberrations of the VAMOS++ spectrometer: calculated angle (θ_f) as a function of the positions (x_f) at the image focal plane of VAMOS++ illustrating effects of aberrations in position and angle. The figure shows the final positions of the trajectories for discrete relative rigidity ($\delta = B\rho/B\rho_0$) varied in 2% step and horizontal angle θ_i by 10 mrad. The arrow shows the increasing $B\rho$ direction. The trajectories, whose vertical angle $\phi_i = 0$ mrad are indicated by triangles, $\phi_i = \pm 50$ mrad by circles and $\phi_i = \pm 100$ mrad by squares. The arrow across the figure represents the positions of central rays with $\theta_i = 0$ mrad. The inset shows a zoom in the region of low $B\rho$. The horizontal position of the physical segments of the MWPCFP located in the focal plane is also indicated.

field. The final coordinates of the trajectories are calculated on the image focal plane located 7600 mm away from the target. For each trajectory, its initial trajectory vector $\vec{l}_i = (0, \theta_i, 0, \phi_i, 0, \delta_i)$ and final trajectory vector $\vec{l}_f = (x_f, \theta_f, y_f, \phi_f, l_f, \delta_f)$, are stored, provided that the trajectory reaches the image plane of VAMOS++. It should be noted that $\delta_i = \delta_f$.

The optics of the VAMOS spectrometer was designed to have the horizontal plane as dispersive plane. In the first order, the dispersion is $\sim 2\text{cm}/\%$. The horizontal coordinates in the dispersive plane are dominantly decoupled and thus independent of the vertical coordinates. This can be seen in the Fig. 2, where the dependence on vertical coordinate (ϕ_i) is limited. The horizontal position of the beam at the target, in the first order, results in a proportional position displacement in the focal plane ($\delta x_i \propto \delta x_f$). Therefore, in the first order, the horizontal size of the beam spot of ~ 2 mm would result in $\sim 1\%$ uncertainty in the magnetic rigidity.

To illustrate the non-linearity in the ion-optics of VAMOS++ the calculated θ_f as a function of x_f in the image focal plane of VAMOS++ is shown in Fig. 2. Overall effect of aberrations in position and angle can be seen in the figure. The impact on the horizontal image, due to the non-null vertical coordinate ϕ_i , is also indicated. The triangles corresponding to the trajectories with $\phi_i = 0$ mrad delimit a full $B\rho - \theta_i$ acceptance phase space of VAMOS++. The circles $\phi_i = \pm 50$ mrad and squares $\phi_i = \pm 100$ mrad indicate the complex 3-dimensional $(B\rho - \theta_i - \phi_i)$ acceptance

phase space. It is interesting to notice, that in the region of the low relative $B\rho$

- in the first order $B\rho$ is proportional to x_f ,
- the ions with large $|\phi_i|$ are accepted for small $|\theta_i|$ and are progressively lost for larger $|\theta_i|$.

In the region of the high relative $B\rho$

- in the first order $B\rho$ is proportional to θ_f ,
- the ions with large $|\phi_i|$ are accepted for large $|\theta_i|$ and are progressively lost for smaller $|\theta_i|$.

Finally, the difference in position between the corresponding points $\phi_i = 0, \pm 50, \pm 100$ mrad compared to the $B\rho$ step of 2% illustrate the importance of the vertical coordinate in the determination of $\delta B\rho$ resolution in the few per mille limit.

4. Trajectory reconstruction

The goal of the trajectory reconstruction methods described in this section is to provide the high resolution vector $\vec{t}_{rec} = (\theta_i, \phi_i, \delta_i, l_f)$ from measured final or/and initial coordinates on an even-by-event basis. Additionally, the reconstruction methods should be implemented for efficient on-line analysis of data. In the following sections, three different trajectory reconstruction methods will be described and their performances, applied to the same experimental data set, will be discussed.

4.1. The Polynomial approach

In the early years of operation of VAMOS++, the polynomial expansion method was used for the trajectory reconstruction. For each of the experimentally detected ions, the measured coordinates in the image focal plane form a vector of final coordinates $\vec{t}_{exp} = (x_f, \theta_f, y_f, \phi_f)$. Let $m = \theta_i, \phi_i, \delta_i, l_f$ denote four coordinates to be reconstructed forming a vector $\vec{t}_{rec} = (\theta_i, \phi_i, \delta_i, l_f)$. Each of the coordinates m can be expressed as independent non-linear function $m = F_m(x_f, \theta_f, y_f, \phi_f)$. It used only the final focal plane coordinates. Its 7th order implementation is described in Ref. [1]. This method was suitable for measurements involving the relatively light ions $A < 70$ [17–19]. For heavier ions the 10th order polynomial expansion method was introduced in 2008. The 10th order polynomial expansion method will be detailed in this section.

The four non-linear inverse transfer functions F_m can be expressed as a 10th order polynomial of four variables $(x_f, \theta_f, y_f, \phi_f)$, measured exclusively in the image focal plane of VAMOS++. The inverse transfer function F_m can be expressed as:

$$F_m = \sum_{i,j,k,l=0}^{i+j+k+l=10} C_{m_{ijkl}} (x_f)^i (\theta_f)^j (y_f)^k (\phi_f)^l \quad (1)$$

where the coefficients $C_{m_{ijkl}}$ are related to the properties of the inverse transfer map of the system. The unknown coefficients $C_{m_{ijkl}}$ can be determined numerically. A computer program was developed for this purpose. It uses the set of trajectories computed by ZGOUBI, as described in Sec. 3, and determines the best converged solution for $C_{m_{ijkl}}$ by fitting the polynomial expression in an iterative procedure. The initial trajectories have been calculated in steps of $d\theta_i = 10$ mrad, $d\phi_i = 10$ mrad and $d\delta_i = 5 \times 10^{-3}$. It should be noted that due to mid plane symmetry in the system, the coefficients $C_{m_{ijkl}}$ are null for θ_i, δ_i and l_f for odd values of $k+l$ and for ϕ_i for even values of $k+l$. The remaining number of non-null coefficients for θ_i, δ_i and l_f is 511 and for ϕ_i is 490. Once the $C_{m_{ijkl}}$ coefficients were determined, they were used for the reconstruction algorithm to map the measured final coordinates data on an event-by-event basis. Since the algorithm is independent of any optics code once the coefficients are fixed, it can easily be adopted in both on-line and offline event identification. It should be noted that the VAMOS++ vertical magnification is of about 7 in first order and that the finite vertical beam spot size induces a large uncertainty of the reconstructed values of θ_i, δ_i and l_f . Therefore, the reconstruction of θ_i, δ_i and l_f were obtained solely from $F_m(x_f, \theta_f, 0, 0)$ while the reconstruction of ϕ_i was obtained from $F_m(x_f, \theta_f, y_f, \phi_f)$.

4.2. Two-dimensional (2D) mapping

The 10th order polynomial approach, despite its complexity, is unable to account for all the details of the aberrations with a single set of coefficients for the whole focal plane. This results in reduced resolution of the reconstructed θ_i, δ_i and l_f . Attempts to overcome this limitation by sub-dividing the focal plane phase space for the polynomial approach did not result in significant improvement in the atomic mass resolution. Therefore, the two-dimensional (2D) mapping approach was introduced in 2011 while increasing the size of the focal plane detection [2].

Let the coordinates $m = \theta_i, \delta_i, l_f$ be reconstructed using only the final image focal plane coordinates x_f, θ_f and the reconstruction of the coordinate ϕ_i remain as in the polynomial approach, Sec. 4.1. The values of each of the m coordinates can be stored in the two-dimensional array M_m , as unsigned 2-byte integer, with the numerical precision of 10^{-3} , 1 mrad and 1 mm for δ_i, θ_i and l_f , respectively. The dimensions of each array M_m were chosen to be 1100×550 corresponding to steps of 1 mm and 1 mrad for the coordinates x_f and θ_f , respectively. Every of the arrays M_m occupies ~ 1.15 Mb of RAM. The initial trajectories have been calculated in steps of $d\theta_i = 0.05$ mrad, $d\phi_i = 20$ mrad and $d\delta_i = 2 \times 10^{-4}$, for initial coordinates. The step size have been chosen to ensure a continuity of the arrays M_m . For each calculated trajectory the δ_i, θ_i and l_f coordinates were stored in the M_m arrays, as a

function of x_f and θ_f coordinates, as follows:

$$\begin{aligned} k &= \lfloor x_f + 600 + 0.5 \rfloor \\ l &= \lfloor \theta_f + 200 + 0.5 \rfloor \end{aligned}$$

$$\begin{aligned} M_{\delta_i}[k][l] &= \lfloor \delta_i \times 1000 + 0.5 \rfloor \\ M_{\theta_i}[k][l] &= \lfloor \theta_i + 200 + 0.5 \rfloor \\ M_{l_f}[k][l] &= \lfloor l_f + 0.5 \rfloor \end{aligned}$$

where: x_f and l_f are in mm and θ_i and θ_f are in mrad. The inverse procedure to obtain reconstructed parameters from measured (x_f, θ_f) is straightforward.

4.3. Four-dimensional (4D) mapping

The further improvement of the reconstruction quality was one of the reasons to build the DPS-MWPC [74], shown in Fig. 1(b). DPS-MWPC placed at the entrance of VAMOS++ provides the two-fold time measurement as well as two-fold vertical and horizontal position leading thus the scattering angles θ_i, ϕ_i and the interaction point at the target x_i, y_i . Typical resolutions of the reconstructed angles and positions on the target were reported in Ref. [74] to be $\sigma = 1.1$ (1) mrad and $\sigma = 239$ (30) μm um respectively.

The four-dimensional (4D) mapping method, introduced in 2016, is an extension of the 2D mapping, where in addition the final image plane coordinates x_f, θ_f , the initial coordinates ϕ_i, θ_i will also be used. The reconstructed coordinates will be $m = \delta_i, l_f$. The values of each of the m coordinates can be stored in the four-dimensional array M_m , as unsigned 2-byte integer, with a numerical precision of 10^{-3} and 1 mm for δ_i and l_f , respectively. The dimensions of each array M_m were chosen to be $960 \times 450 \times 180 \times 260$, steps of 1 mm, 1 mrad, 2 mrad and 1 mrad, for coordinates x_f, θ_f, ϕ_i and θ_i , respectively. Both arrays M_m have a total memory requirement of ~ 75 Gb. The initial trajectories have been calculated in steps of $d\theta_i = 0.05$ mrad, $d\phi_i = 2$ mrad and $d\delta_i = 1 \times 10^{-4}$, for initial coordinates. The step size has been chosen such to guarantee a continuity of the arrays M_m . For each calculated trajectory the δ_i and l_f were stored in the M_m arrays as a function of the x_f, θ_f, ϕ_i and θ_i coordinates, as follows:

$$\begin{aligned} k &= \lfloor x_f + 550 + 0.5 \rfloor \\ l &= \lfloor \theta_f + 200 + 0.5 \rfloor \\ m &= \lfloor \phi_i/2 + 90 + 0.5 \rfloor \\ n &= \lfloor \theta_i + 130 + 0.5 \rfloor \end{aligned}$$

$$\begin{aligned} M_{\delta_i}[k][l][m][n] &= \lfloor \delta_i \times 1000 + 0.5 \rfloor \\ M_{l_f}[k][l][m][n] &= \lfloor l_f + 0.5 \rfloor \end{aligned}$$

where: x_f and l_f are in mm and θ_i, θ_f and ϕ_i are in mrad. VAMOS++ acceptance phase space makes the M_m

arrays relatively sparse. The application of a zero suppression algorithm, compressed row storage (CRS) [77] allows to reduce the total required memory size from ~ 75 Gb to ~ 1 Gb. To further facilitate the memory usage, the compressed arrays can be stored in a binary format on disk and read into a permanent shared memory segment made available for several analysis programs/processes at the same time.

It should be noted that, contrary to the polynomial and two-dimensional methods, the four-dimensional method does not ensure that every input vector $(x_f, \theta_f, \phi_i, \theta_i)$ results in a valid M_m . This is due to the limited phase space of the spectrometer. This feature will be discussed in the following section and outlook.

5. Experimental results

In this section, the different methods are applied to a common benchmark experimental dataset and the performances in terms of reconstructed atomic mass are compared and discussed. The experimental dataset arise from an experiment performed at GANIL, where the fission fragments were produced in fusion and transfer induced fission reactions using a ^{238}U beam at the energy of 6.2 MeV/u on a ^9Be target (1.6 and 5 μm thick). A schematic view of the experimental setup is shown in Fig. 1(a). The VAMOS++ spectrometer was placed at 20° relative to the beam axis. Further detail can be found in Ref. [6].

The results will be first illustrated using the data obtained from the physical section number 4 of the MWPC detector of the focal plane. In Fig. 3 the correlation between the atomic charge state q and the mass-over-charge ratio (A/q) is shown. Panels (a), (b) and (c) show the comparison of the results of the polynomial approach, the two-dimensional and four-dimensional mapping, respectively. The gradual improvement of the quality of the identification can be seen. It should be noted that improved (A/q) reconstruction translates in an improved charge state resolution. The spectra of atomic mass number A obtained from four-dimensional mapping method, in red, is compared to that obtained from polynomial approach in blue in Fig. 3(d) and to that obtained using two-dimensional mapping in blue in Fig. 3(e). It can be seen from the figures that atomic mass resolution ($\Delta A_{FWHM}/A$) is significantly improved by using the four-dimensional mapping. The resolution for $A = 100$ is found to be 5‰ for the four-dimensional mapping compared to 7.5‰ for the polynomial approach and 6‰ for the two-dimensional mapping. This correspond respectively to 50% and 20% improvement of the atomic mass resolution for this region of the VAMOS++ focal plane.

It can be seen in Fig. 2 that the optical aberrations of VAMOS++ change as a function of the magnetic rigidity $B\rho$ of the ion and thus also as a function of the x_f image plane coordinate. It has been observed that the differences between the results of different reconstruction methods are the largest in the region of low relative $B\rho$.

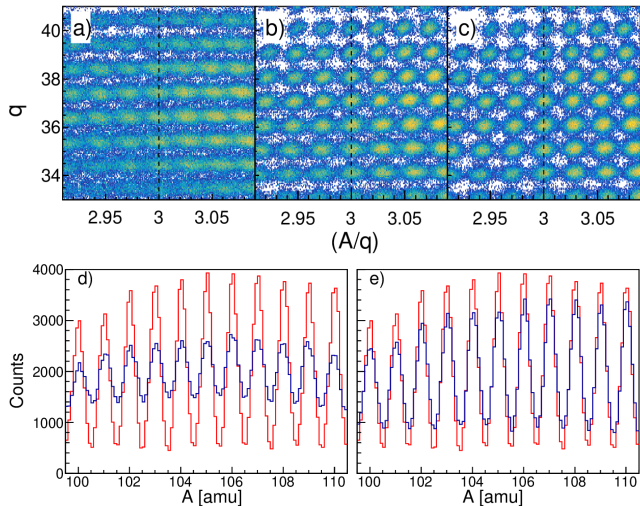


Figure 3: Atomic charge state (q) as a function of mass-over-charge ratio (A/q) for physical section number 4 of the MWPCFP ($250\text{mm} < x_f < 300\text{mm}$) using different reconstruction methods a) polynomial approach, b) 2D mapping, c) 4D mapping. The atomic mass number A using 4D mapping in red compared to d) polynomial approach and e) 2D mapping methods in blue.

In section number 10 (see Fig. 2), polynomial approach and two-dimensional mapping were found to be equivalent and the four-dimensional resulted in a 10% improvement yielding to an atomic mass resolution of 6‰ for $A = 100$. In section number 16, the three approaches are found to give equivalent atomic mass resolution. This can be explained by the fact that for higher magnetic rigidity, the ions have in average higher velocity and the contribution of the time of flight resolution in the atomic mass resolution dominates.

Further, the atomic mass number spectrum of fission fragments obtained for the complete focal plane is shown in Fig. 4(a). The spectrum shown in red correspond to the four-dimensional mapping reconstruction and the spectrum shown in blue to that of the two-dimensional mapping. Figure 4(b) shows the associated FWHM resolution obtained for atomic mass number $\Delta A_{FWHM}/A$, in per mille (‰), as a function of A . A clear improvement in width ΔA_{FWHM} of about 8% for the four-dimensional mapping method, relative to other methods, can be seen in the figure. The downward slope of the $\Delta A_{FWHM}/A$ as a function of increasing A results from nearly constant ΔA_{FWHM} .

Finally, the efficiency of the reconstruction method is 100% for polynomial and two-dimensional methods. However, in the case of the four-dimensional method, a typical efficiency of $\sim 97\%$ was obtained. This reduced efficiency can be related to the highly constrained phase space arising from the optics of the spectrometer. As an example, an extension of the beam on target (typically $\Delta x_{FWHM} = 1.2\text{ mm}$ and $\Delta y_{FWHM} = 1.5\text{ mm}$ [74]) will result in some initial angles (θ_i , ϕ_i) residing out of the calculated phase space assuming a point-like beam spot

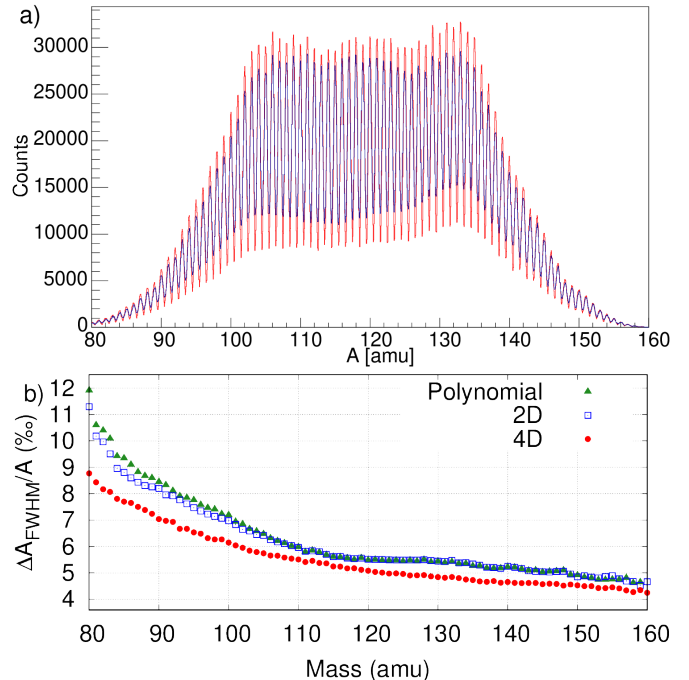


Figure 4: a) Atomic mass number A for events collected using a full image focal plane of VAMOS++, in red 4D mapping method and in blue 2D mapping method. b) Resolution of atomic mass number $\Delta A_{FWHM}/A$ as a function of atomic mass number A for the polynomial (green triangles), two- (open blue squares) and four-dimensional (red circles) reconstruction methods.

($x_i = 0$ and $y_i = 0$). As a consequence, for such cases, the four-dimensional method will not provide reconstructed δ_i and l_f . Nevertheless, the two-dimensional method can be used as a failover solution for these events at the cost of a reduced resolution. The implementation of the reconstruction method accounting for a size of the beam spot is considered for future work. It should be however noted that, the use of such a method on an event-by-event basis, will require an increase of the matrix size at least by a factor of ~ 10 .

6. Summary and perspectives

The large angular and momentum acceptance magnetic spectrometer VAMOS++, is particularly well suited for the studies of nuclear structure and reactions dynamics at the beam energies near the Coulomb barrier. The main objective of VAMOS++ is to provide on an event-by-event basis the isotopic identification of the reaction products of interest. A high-resolution of the atomic mass measurement requires the use of the trajectory reconstruction methods, due to the highly non-linear ion optics of the spectrometer. Three trajectory reconstruction methods have been developed and used in the past years

1. polynomial approach, using x_f , θ_f , y_f and ϕ_f coordinates,

2. two-dimensional (2D) mapping using x_f, θ_f coordinates,
3. four-dimensional (4D) mapping x_f, θ_f and ϕ_i and θ_i coordinates.

These methods makes use of the parameters derived from of set of trajectories of the ions in VAMOS++ calculated using ray-tracing code ZGOUBI [75]. All methods are fast and allow an efficient treatment of the experimental data in an on-line and off-line analysis. The trajectory reconstruction method were applied to a single data-set of fission fragments.

An improvement of about 8% was obtained using 4D mapping method as compared to the polynomial approach and two-dimensional mapping method, leading to $\Delta A_{FWHM}/A$ ranging from 4.5‰ ($\frac{1}{220}$) for heaviest fragments to 9‰ ($\frac{1}{110}$) for lightest fragments.

The trajectory reconstruction methods presented on this work are based on the assumption that the beam spot size at the target is point-like, $x_i = 0$ and $y_i = 0$, while the typical beam spot size is $\Delta x_{FWHM} = 1.2$ mm and $\Delta y_{FWHM} = 1.5$ mm [74]. In future work, it is foreseen to extend the mapping method including the event-by-event measurement of the interaction point on the target and investigate its impact of the resolution of the reconstructed atomic mass number.

Acknowledgements

The authors thank B. Jacquot and D. Ramos for numerous fruitful discussions.

References

References

- [1] S. Pullanhiotan, et al., *Nucl. Instrum. Methods Phys. Res. A* (2008) 343–352 doi:10.1016/j.nima.2008.05.003.
- [2] M. Rejmund, et al., *Nucl. Instrum. Methods Phys. Res. A* (2011) 184–191 doi:10.1016/j.nima.2011.05.007.
- [3] G. Montagnoli, et al., *Nucl. Instrum. Methods Phys. Res. A* (2005) 455–463 doi:10.1016/j.nima.2005.03.158.
- [4] D. Bazin, et al., *Nucl. Instrum. Methods Phys. Res. B* (2003) 629–633 doi:10.1016/S0168-583X(02)02142-0.
- [5] M. Cortesi, et al., *J. Instrum.* (2020) P03025–P03025 doi:10.1088/1748-0221/15/03/P03025.
- [6] Y. H. Kim, et al., *Eur. Phys. J. A* (2017) 162 doi:10.1140/epja/i2017-12353-y.
- [7] A. Obertelli, et al., *Phys. Rev. C* (2006) 064305 doi:10.1103/PhysRevC.74.064305.
- [8] A. Obertelli, et al., *Phys. Lett. B* (2006) 33–37 doi:10.1016/J.PHYSLETB.2005.11.033.
- [9] M. Labiche, et al., *Nucl. Instrum. Methods Phys. Res. A* (2010) 439–448 doi:10.1016/J.NIMA.2010.01.009.
- [10] W. N. Catford, et al., *Phys. Rev. Lett.* (2010) 192501 doi:10.1103/PhysRevLett.104.192501.
- [11] B. Fernández-Domínguez, et al., *Phys. Rev. C* (2011) 011301 doi:10.1103/PhysRevC.84.011301.
- [12] S. M. Brown, et al., *Phys. Rev. C* (2012) 011302 doi:10.1103/PhysRevC.85.011302.
- [13] F. Flavigny, et al., *Phys. Rev. Lett.* (2013) 122503 doi:10.1103/PhysRevLett.110.122503.
- [14] M. Assié, et al., *Nucl. Instrum. Methods Phys. Res. A* (2021) 165743 doi:10.1016/j.nima.2021.165743.
- [15] F. Galtarossa, et al., *Nucl. Instrum. Methods Phys. Res. A* (2021) 165830 doi:10.1016/j.nima.2021.165830.
- [16] V. Girard-Alcindor, et al., *Phys. Rev. C* (2022) L051301 doi:10.1103/PhysRevC.105.L051301.
- [17] M. Rejmund, et al., *Phys. Rev. C* (2007) 021304 doi:10.1103/PhysRevC.76.021304.
- [18] S. Bhattacharyya, et al., *Phys. Rev. Lett.* (2008) 032501 doi:10.1103/PhysRevLett.101.032501.
- [19] S. Bhattacharyya, et al., *Phys. Rev. C* (2009) 014313 doi:10.1103/PhysRevC.79.014313.
- [20] J. Ljungvall, et al., *Phys. Rev. C* (2010) 061301 doi:10.1103/PhysRevC.81.061301.
- [21] A. Dijon, et al., *Phys. Rev. C* (2011) 064321 doi:10.1103/PhysRevC.83.064321.
- [22] A. Dijon, et al., *Phys. Rev. C* (2012) 031301 doi:10.1103/PhysRevC.85.031301.
- [23] I. Celikovic, et al., *Phys. Rev. C* (2015) 044311 doi:10.1103/PhysRevC.91.044311.
- [24] M. Klintejord, et al., *Phys. Rev. C* (2017) 024312 doi:10.1103/PhysRevC.95.024312.
- [25] A. Goldkuhle, et al., *Phys. Rev. C* (2019) 054317 doi:10.1103/PhysRevC.100.054317.
- [26] D. Ralet, et al., *Phys. Lett. B* (2019) 134797 doi:10.1016/j.physletb.2019.134797.
- [27] M. Siciliano, et al., *Phys. Rev. C* (2020) 021303 doi:10.1103/PhysRevC.101.021303.
- [28] A. Goldkuhle, et al., *Phys. Rev. C* (2020) 054334 doi:10.1103/PhysRevC.102.054334.
- [29] M. Siciliano, et al., *Phys. Lett. B* (2020) 135474 doi:10.1016/j.physletb.2020.135474.
- [30] M. Ciemala, et al., *Eur. Phys. J. A* (2021) 156 doi:10.1140/epja/s10050-021-00451-6.
- [31] M. Siciliano, et al., *Phys. Rev. C* (2021) 034320 doi:10.1103/PhysRevC.104.034320.
- [32] S. Ziliani, et al., *Phys. Rev. C* (2021) L041301 doi:10.1103/PhysRevC.104.L041301.
- [33] R. M. Pérez-Vidal, et al., *Phys. Rev. Lett.* (2022) 112501 doi:10.1103/PhysRevLett.129.112501.
- [34] A. Shrivastava, et al., *Phys. Rev. C* (2009) 051305 doi:10.1103/PhysRevC.80.051305.
- [35] A. Navin, M. Rejmund, Gamma-ray spectroscopy of neutron-rich fission fragments, in: *McGRAW-HILL Yearb. Sci. Technol.*, 2014, p. 137. doi:10.1036/1097-8542.YB140316.
- [36] A. Navin, et al., *Phys. Lett. B* (2014) 136–140 doi:10.1016/j.physletb.2013.11.024.
- [37] E. H. Wang, et al., *Phys. Rev. C* (2015) 034317 doi:10.1103/PhysRevC.92.034317.
- [38] S. Biswas, et al., *Phys. Rev. C* (2016) 034324 doi:10.1103/PhysRevC.93.034324.
- [39] M. Rejmund, et al., *Phys. Lett. B* (2016) 86–90 doi:10.1016/j.physletb.2015.11.077.
- [40] M. Rejmund, et al., *Phys. Rev. C* (2016) 024312 doi:10.1103/PhysRevC.93.024312.
- [41] T. W. Hagen, et al., *Phys. Rev. C* (2017) 034302 doi:10.1103/PhysRevC.95.034302.
- [42] Y. Kim, et al., *Phys. Lett. B* (2017) 403–408 doi:10.1016/j.physletb.2017.06.058.
- [43] A. Navin, et al., *Phys. Lett. B* (2017) 480–484 doi:10.1016/j.physletb.2016.11.020.
- [44] J. Dudouet, et al., *Phys. Rev. Lett.* (2017) 162501 doi:10.1103/PhysRevLett.118.162501.
- [45] T. W. Hagen, et al., *Eur. Phys. J. A* (2018) 50 doi:10.1140/epja/i2018-12482-9.
- [46] S. Bhattacharyya, et al., *Phys. Rev. C* (2018) 044316 doi:10.1103/PhysRevC.98.044316.
- [47] C. Delafosse, et al., *Phys. Rev. Lett.* (2018) 192502 doi:10.1103/PhysRevLett.121.192502.
- [48] P. Singh, et al., *Phys. Rev. Lett.* (2018) 192501 doi:10.1103/PhysRevLett.121.192501.

- [49] J. Dudouet, et al., *Phys. Rev. C* (2019) 011301 doi:10.1103/PhysRevC.100.011301.
- [50] S. Biswas, et al., *Phys. Rev. C* (2019) 064302 doi:10.1103/PhysRevC.99.064302.
- [51] S. Biswas, et al., *Phys. Rev. C* (2020) 014326 doi:10.1103/PhysRevC.102.014326.
- [52] R. Banik, et al., *Phys. Rev. C* (2020) 044329 doi:10.1103/PhysRevC.102.044329.
- [53] E. H. Wang, et al., *Phys. Rev. C* (2021) 034301 doi:10.1103/PhysRevC.103.034301.
- [54] K. Rezynkina, et al., *Phys. Rev. C* (2022) 014320 doi:10.1103/PhysRevC.106.014320.
- [55] C. Plaisir, et al., *Phys. Rev. C* (2014) 021302 doi:10.1103/PhysRevC.89.021302.
- [56] M. Caamaño, et al., *Phys. Rev. C* (2013) 024605 doi:10.1103/PhysRevC.88.024605.
- [57] C. Rodriguez-Tajes, et al., *Phys. Rev. C* (2014) 024614 doi:10.1103/PhysRevC.89.024614.
- [58] F. Farget, et al., *Eur. Phys. J. A* (2015) 175 doi:10.1140/epja/i2015-15175-y.
- [59] M. Caamaño, et al., *Phys. Rev. C* (2015) 034606 doi:10.1103/PhysRevC.92.034606.
- [60] M. Caamaño, F. Farget, *Phys. Lett. B* (2017) 72–76 doi:10.1016/j.physletb.2017.04.041.
- [61] D. Ramos, et al., *Phys. Rev. C* (2018) 054612 doi:10.1103/PhysRevC.97.054612.
- [62] D. Ramos, et al., *Phys. Rev. C* (2019) 024615 doi:10.1103/PhysRevC.99.024615.
- [63] D. Ramos, et al., *Phys. Rev. Lett.* (2019) 092503 doi:10.1103/PhysRevLett.123.092503.
- [64] D. Ramos, et al., *Phys. Rev. C* (2020) 034609 doi:10.1103/PhysRevC.101.034609.
- [65] C. Schmitt, et al., *Phys. Rev. Lett.* (2021) 132502 doi:10.1103/PhysRevLett.126.132502.
- [66] A. Jhingan, et al., *Phys. Rev. C* (2022) 044607 doi:10.1103/PhysRevC.106.044607.
- [67] G. Benzoni, et al., *Eur. Phys. J. A* (2010) 287–292 doi:10.1140/epja/i2010-11011-4.
- [68] C. Golabek, et al., *Eur. Phys. J. A* (2010) 251–259 doi:10.1140/epja/i2010-10911-5.
- [69] Y. X. Watanabe, et al., *Phys. Rev. Lett.* (2015) 172503 doi:10.1103/PhysRevLett.115.172503.
- [70] P. Marini, et al., *Phys. Lett. B* (2016) 194–199 doi:10.1016/j.physletb.2016.02.063.
- [71] Q. Fable, et al., *Phys. Rev. C* (2022) 024605 doi:10.1103/PhysRevC.106.024605.
- [72] Q. Fable, et al., *Phys. Rev. C* (2023) 014604 doi:10.1103/PhysRevC.107.014604.
- [73] A. Drouart, et al., *Nucl. Instrum. Methods Phys. Res. A* (2007) 1090–1095 doi:10.1016/j.nima.2007.05.202.
- [74] M. Vandebrouck, et al., *Nucl. Instrum. Methods Phys. Res. A* (2016) 112–117 doi:10.1016/j.nima.2015.12.040.
- [75] F. Méot, *Nucl. Instrum. Methods Phys. Res. A* (1999) 353–356 doi:https://doi.org/10.1016/S0168-9002(98)01508-3.
- [76] TOSCA Static Field Analysis OPERA-3D.
- [77] R. Barrett, et al., *Templates for the Solution of Linear Systems: Building Blocks for Iterative Methods*, Society for Industrial and Applied Mathematics, 1994. doi:10.1137/1.9781611971538.